Journal of Radioanalytical and Nuclear Chemistry (2018) 318:1389–1400
https://doi.org/10.1007/s10967-018-6232-3

Characterization of uraninite using a FIB–SEM approach and its implications for LA–ICP–MS analyses

Stefanie R. Lewis[1] · Antonio Simonetti[1] · Loretta Corcoran[1] · Tyler L. Spano[1] · Brandon W. Chung[2] · Nick E. Teslich[2] · Peter C. Burns[1,3]

Received: 23 July 2018 / Published online: 6 October 2018

Abstract
Focused ion beam (FIB) coupled with scanning electron microscopy (SEM) investigations were performed on pristine and altered areas of two uraninite samples in order to better understand their 3-dimensional mineralogical and chemical nature, and their impact on trace element abundances obtained by laser ablation inductively coupled plasma mass spectrometry (LA–ICP–MS) analyses. Trace element contents determined by both LA- and solution mode (SM)–ICP–MS analyses together with FIB results identify Pb as the optimal internal standard for LA–ICP–MS analyses of uraninite since it is a major chemical constituent, part of the structure, and similar in abundance to the trace elements of interest.

Keywords Uraninite · Nuclear forensics · Focused ion beam · Laser ablation · Inductively coupled plasma mass spectrometry · Trace elements

Introduction

The main constituent mineral of viable uranium ore deposits is uraninite (UO_{2+x}), which is an indispensable raw material used for the fabrication of nuclear fuel bound for reactors. Uraninite has the capacity to incorporate elemental impurities resulting in a diverse chemical composition; thus a more representative formula is $(U^{4+}_{1-x-y-z-u}U^{6+}_{x}REE^{3+}_{y}M_{z}^{2+}\square^{4-}_{u})O_{2+x-0.5y-z-2u}$, where M are divalent metal ions and □ represents a vacancy [1]. Uranium deposits are found on most continents and classified according to their host rock lithology, nearby tectonic structures, and mode of alteration [2]. As naturally-occurring nuclear material, uraninite has the potential of being illegally obtained or illicitly traded. For deterrence purposes, various analytical techniques are implemented to fully characterize the raw material for provenance examination and identifying industrial history. For example, the generation of an inclusive data base allowing deposit type identification based on their trace element [3, 4] and/or isotopic signatures [5, 6].

In previous studies of nuclear materials [6–9], incorporation of the rare earth elements (REEs) has been established as a key forensic indicator for source attribution. By normalizing abundances of REEs for samples to chondritic concentrations, the resulting shape of the REE pattern is characteristic of the specific U deposit, which has been influenced by temperature, fluid chemistry, and source of the REEs [3, 7].

The majority of previous investigations of nuclear materials have reported chemical data determined using conventional bulk digestion of samples, often taking days to complete. Recent advances in analytical techniques, such as the development of laser ablation–inductively coupled plasma mass spectrometry (LA–ICP–MS), yields the possibility of obtaining highly precise and accurate trace element abundances at high spatial resolution in an expedited manner (within hours; [4, 10, 11]). The accuracy

Electronic supplementary material The online version of this article (https://doi.org/10.1007/s10967-018-6232-3) contains supplementary material, which is available to authorized users.

✉ Stefanie R. Lewis
Stefanie.R.Lewis.184@nd.edu

[1] Department of Civil and Environmental Engineering and Earth Sciences, University of Notre Dame, Notre Dame, IN 46556, USA

[2] Lawrence Livermore National Laboratory, P.O. Box 808, Livermore, CA 94551, USA

[3] Department of Chemistry and Biochemistry, University of Notre Dame, Notre Dame, IN 46556, USA

and reliability of chemical data obtained by LA–ICP–MS analyses is dependent on identifying the most appropriate element for use as the internal standard. The latter monitors instrumental drift and matrix effects, i.e., providing time-sensitive normalization factors based on the measured ion yield (ion signal in counts per second—cps/concentration) for the internal standard within the external standard; the latter is then compared to the ion yield for the same element in the unknowns. The internal standard abundance (typically wt%) is usually determined by electron microprobe (EMP) analysis, and it must be present within both the external standard and the unknowns. Moreover, when choosing an appropriate internal standard, it is critical that the element of choice is incorporated within the mineral's crystal structure and not part of a secondary (alteration/exsolution) phase. The high resolution (10–100 s of micron scale) nature of LA–ICP–MS analyses records trace element data within the spatial context of samples, which is information that bulk digestions overprint. This spatial context is vital for the determination of trace element abundances within micrometer overgrowths, or zoning textures developed during crystallization and/or alterations [12].

Lach et al. [12] previously investigated the use of various internal standards for LA–ICP–MS analyses of uraninite with the conclusion that U was the optimal choice. The extremely high abundance of U (> 90 wt%) relative to those for the remaining elements within uraninite, in particular the REEs and other trace elements of interest, renders its choice as the internal standard somewhat problematic due to the discrepant magnitude in their measured ion signals. Previous studies have used U [3, 13], whereas others have consequently utilized Th or Ca as the internal standard for LA–ICP–MS analyses [8], since both elements substitute for U in the uraninite structure due to their similar ionic radii. However, the abundances of Ca and/or Th are variable and dependent on the U ore deposit type with those that formed at lower temperature, such as metamorphite/hydrothermal deposits typically contain minor amounts of both elements [14]. For example, uraninite from the Great Bear metamorphite deposit (Canada), averages < 1 wt% CaO and ThO_2, whereas uraninite from a pegmatitic intrusive locality such as Mitchell County (USA) averages 1.5 wt% CaO and 5.4 wt% ThO_2.

The aim of this study is to identify an optimal internal standard for use in LA–ICP–MS analysis of uraninite with the assistance of the FIB–SEM (focused ion beam–scanning electron microscopy) technique. A major application for FIB is the preparation for subsequent site-specific transmission electron microscopy (TEM) foil; however, additional uses of this technique have been reported [15]. Here, a first-time micron-scale investigation of uraninite involving a combined FIB–SEM approach will provide critical information in relation to the texture and chemistry of uraninite in the third (vertical profile) dimension. This is an important consideration for LA–ICP–MS investigations given that a typical analysis penetrates a sample to a depth of 50–100 microns [16, 17].

Materials

All uraninite samples analyzed in this study are from the "Ewing Collection" housed at the University of Notre Dame. Seven samples are from locations throughout North America and one from Shinkolobwe, Democratic Republic of the Congo (Table 1). The samples represent three distinct deposit types according to the 2016 IAEA Classification: metamorphite, intrusive non-granite related, and collapsed breccia [2, 6], which are briefly described below.

Metamorphite U deposits contain disseminated veins, impregnations, and shear zones of metamorphic rocks unrelated to granite (Great Bear, Shinkolobwe, Marshall 1, and Marshall 2). The Great Bear uraninite sample is from the Great Bear Lake region of Northwest Territories (Canada), and is located within late Aphebian-aged units comprised of pumice-dominated pyroclastic flows with subordinate ash and plutons. U–Ag–Bi–Cu–Co–Ni–As minerals are found within quartz and carbonate gangue. Hypogene uranium originates from the margin of the Great Bear pre-batholithic placer followed by several remobilization events [18]. The diabase intrusion at Echo Bay is the likely cause for the remobilization and re-precipitation of uraninite [19, 20].

Shinkolobwe uraninite is from the Shinkolobwe Mine (Democratic Republic of the Congo), part of the Shaban area of the Katanga system, known for its U, Cu, Co and Ni ore deposits. Uraninite is found within fractures of dominantly siliceous dolomite, and dolomitic and carbonaceous shales partially affected by Mg-metasomatism. The mine is located near a fold axis hinge where beds start to overturn as part of the Lufilian fold-thrust belt [19, 20].

The two remaining metamorphite-type uraninite samples, Marshall 1 and Marshall 2, can be sub-categorized as hydrothermal deposits due to their genetic classification, i.e., the transport and deposition of uranium by specific chemical and physical environments [2, 21]. Marshall 1 and Marshall 2 are from Marshall Pass, Colorado (USA) where colloform and fine-grained uraninite is formed as a result of hydrothermal activity. In this deposit, uraninite occurs within fault-controlled veins and breccia zones of Pennsylvanian-aged limestone. The uranium ore is found at intersections of major faults where crystalline Proterozoic rocks protrude westward over Paleozoic sequences [14, 22].

Table 1 A list of the uraninite samples investigated with their source location and associated deposit type

Location	Name	Type
Mitchell Co, North Carolina	Mitchell	Intrusive-pegmatite
Ruggles Mine, Grafton, NH	Ruggles	Intrusive-pegmatite
Billiken Lode, Critchell, Jefferson County, CO	Billiken	Intrusive-non-granite related
Shinkolobwe, Congo	Shinkolobwe	Metamorphite
Marshall Pass area, Gunnison County, Colorado	Marshall 1	Metamorphite–hydrothermal
Marshall Pass, Colorado	Marshall 2	Metamorphite–hydrothermal
Great Bear Lake, NWT, Canada	Great Bear	Metamorphite
Orphan Lode, Grand Canyon, AZ	Orphan	Collapsed breccia

Three uraninite samples are classified as intrusive, non-granite related (Billiken, Mitchell, and Ruggles), and are related to anatectic or plutonic activity [2, 6]. The Billiken uraninite is from Billiken Lode, Jefferson County (Colorado, USA), and is hosted by complexly folded and faulted Proterozoic metasediments situated between two major faults; accessory minerals include ankerite, quartz, calcite, and potassium feldspar [14, 20].

The remaining intrusive uraninite samples from Mitchell County (North Carolina, USA) and Ruggles Mine in Grafton County (New Hampshire, USA) investigated here are sub-classed as pegmatitic due to their relation to late-stage magmatism. The Mitchell uraninite is hosted by the Spruce Pine pegmatite, which crosscuts the surrounding SW plunging asymmetrical syncline of interlayered mica and amphibole gneiss and schist of Precambrian age. The emplacement of this pegmatite is linked with the closing of the Proto-Atlantic Ocean [23]. The Ruggles uraninite is associated with a zoned pegmatite of Devonian age within the Littleton Formation, and occurs as dendritic intergrowths within irregular bodies of quartz and late veins adjacent to the perthite core [24, 25]. The host rock consists of quartz–mica schist, quartzite, amphibolite, and other high grade metamorphic rocks [24, 26].

The uraninite from Orphan Lode (Arizona, USA) located within the Grand Canyon National Park represents a sample from a collapsed breccia pipe. The uranium is found almost entirely within the collapse breccia structure disseminated within the host rock matrix (limestone, sandstone, and shale of Pennsylvanian and Permian age), and as arched fracture zones around the pipe [27, 28].

Each uraninite sample was cut into small portions $\sim$ 1 cm^2 in size and placed with a fresh cut surface down into a 1-inch round mount, filled with epoxy and cured before being polished. Trace element concentrations for all samples (Supplementary Table 2) were determined using LA–ICP–MS with two samples (Ruggles and Marshall 2) being examined by FIB. These two samples were selected to compare the structure and chemistry of pristine (Ruggles) versus altered (Marshall 2) uraninite. The uraninite at Ruggles occurs as well-defined dendritic nodules in which all uraninite is characterized as pristine (> 80 wt% UO_2). In contrast, the Marshall 2 uraninite is characterized by distinct fan-shape morphology and is surrounded by alteration rinds and secondary minerals formed during late-stage hydrothermal activity.

Methods

Micro-X-ray fluorescence (μ-XRF)

Elemental maps were produced using an EDAX Orbis Micro EDXRF with the following conditions: 40 kV voltage, 300 μA, and 100 μs dwell time. The μ-XRF elemental maps provide a qualitative assessment of the chemical composition of individual samples, and vital information for determining the locations of interest for subsequent electron microprobe (EMP) and LA–ICP–MS analyses (Fig. 1).

Electron microprobe (EMP)

Polished sample mounts were carbon coated prior to EMP analyses and FIB investigations. Major element analyses were performed using a Cameca SX-50 electron microprobe. Standard operating conditions included an accelerating voltage of 15 kV, a beam current of 100 nA, and a beam size of $\sim$ 3 μm. Elemental oxide abundances (wt%) were determined for 16 elements: U, Pb, Th, Si, Fe, Al, Mn, Ti, As, V, Ca, Zr, K, P, S, and Y. In house standards of UO_2, pyrite, ThO_2, zircon, manganese-hortonolite, anorthite glass, Mn metal, TiO_2, arsenic, V_2O_3, K-feldspar, phosphate, and Y–Al garnet were used for calibration purposes. EMP results provide wt% abundances required for laser ablation (i.e., abundance of internal standard) in addition to determining areas of pristine and altered uraninite, and locations with secondary U-minerals within each sample.

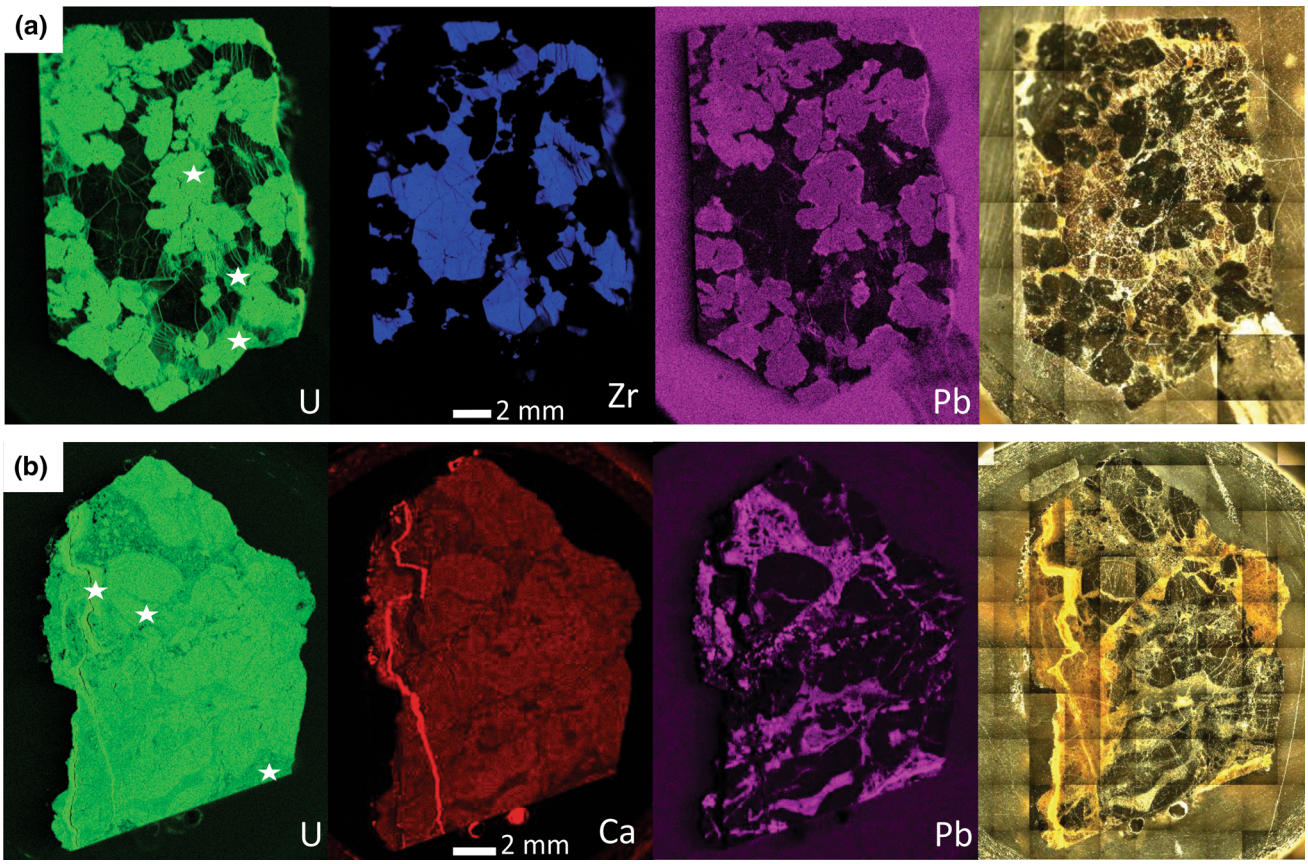

Fig. 1 Micro-XRF elemental maps and corresponding sample mount images taken in plane light of uraninite samples. White stars on the uranium element maps indicate the locations of FIB–SEM investigations **a** Ruggles, **b** Marshall 2. Solely areas with corresponding Pb and U concentrations were studied here as these represent uraninite and/or U-bearing minerals (e.g., secondary alteration phases). For example, the Ruggles sample contains zircon as denoted by the Zr chemical map and these areas were not examined in this study

Laser ablation (LA)–ICP–MS

Trace element abundances were determined using a New Wave Research UP213 Nd:YAG laser ablation system coupled to a Thermo Finnigan Element 2 sector field high resolution (HR)–ICP–MS. Analyses were conducted using a repetition of 5 Hz, an energy density $\sim$ 12 J cm^{-2}, and a 30 µm diameter spot. Background measurements of ion signals were determined for 30 s followed by 60 s of sample ablation. A standard-sample bracketing technique was employed using NIST SRM 610 glass wafer as the external standard. Data reduction including calculations of elemental concentrations, detection limits, and in-run precision were conducted using the GLITTER© software [29] based upon EMP analyses for the internal standard.

Solution mode (SM)–ICP–MS

Aliquots from each uraninite sample were separated, powdered, and digested for solution mode analyses. When possible, samples were separated optically based on color, morphology, and luster before being powdered to establish "pristine" and "altered" fractions. For example, lustrous black portions were deemed pristine sections of samples, whereas yellow and orange sections were considered altered uraninite and/or secondary-U minerals. Approximately 50 mg of powdered sample was placed into 15 ml, pre-cleaned Savillex© Teflon beakers for digestion with $\sim$ 4 ml of double distilled, concentrated HNO_3 acid. Solution mode (SM) analyses were conducted on a Nu Instruments Attom high resolution (HR)–ICP–MS operating at medium mass resolution (M/ΔM $\approx$ 2500). A standard-spike addition method was used to correct for matrix effects and instrumental drift (after [30]).

Focused ion beam (FIB)–secondary electron microscopy (SEM)

FIB–SEM analyses were conducted using a FEI Helios 600i DualBeam FIB–SEM housed within Physical and Life Sciences (PLS) Characterization Directorate at Lawrence Livermore National Laboratory. An ion beam was used to produce a Pt deposition layer that acted as a protective barrier for the sample during the milling process. A gallium

ion beam milled trenches for several locations within uraninite samples from Marshall 2 and Ruggles. Initial milling and final polishing were conducted at 21 and 1 nA, respectively. The samples were then placed at a 52° tilt and imaged using the SEM, and EDS was employed for qualitative determination of elemental concentrations.

Results

Major element abundances obtained by EMP analyses were used to delineate areas of pristine versus altered uraninite, and/or the presence of secondary uranium minerals. The analyses were subsequently grouped according to their UO_2 wt% contents: pristine at > 80 wt%, altered at 79–70 wt%, and two categories for locations with secondary U-minerals at 69–46 and < 45 wt%. LA–ICP–MS analyses were conducted throughout each sample, and within the GLITTER software eight elements (Pb, Th, Ca, Ti, As, Y, Zr, and Mn) were sequentially adopted off-line as the internal standard; calculated trace element concentrations were then compared for each analysis. REE concentrations were then normalized to chondritic abundances (CN = chondrite normalized). In order to eliminate spurious results, the comparison is based on the median (and not the average) value determined for each element of every sample using the different internal standards (Fig. 2). The CN–REE plots show the variability in the calculated absolute concentrations, but the relative abundances remain constant resulting in similar shaped patterns (Fig. 2). However, several samples exhibit slightly different relative abundances for La and Ce (Fig. 2a, c–e), which may be attributed to space charge effects (e.g., [12]). The CN–REE patterns based on the LA–ICP–MS analyses are also compared with data obtained from bulk SM–ICP–MS measurements for each sample (Figs. 2, 3). In order to better understand how the CN–REE patterns vary as a function of the degree of alteration, LA–ICP–MS analyses were grouped into the four UO_2 wt% categories listed above while using Pb as the internal standard (Fig. 3).

In addition to documenting the REE abundances, the concentrations of several other trace elements were obtained by both LA- and SM–ICP–MS (Supplementary Tables 2 and 3). The concentrations of selected trace elements of geochemical importance (Fig. 4) were again determined by varying the choice of the internal standard. Figure 4 demonstrates that apart from Zr and Nb, the calculated abundances of the remaining trace elements define constant ratios, i.e., yield linear arrays relative to one another.

A total of six FIB cross-sections and SEM images were collected for Ruggles (Fig. 5a–c) and Marshall 2 uraninite (Fig. 5d–f). Figure 5c, f denotes SEM images of the FIB cross-sections in relation to their location on the sample surface. SEM images display variable textures and levels of brightness below the sample surface. The latter feature, or light versus dark grey color, is a function of compositional differences; i.e., areas characterized by a heavier mean atomic weight of elements present are brighter or display a lighter grey color. EDS spectra were collected throughout the trench cross-section for a qualitative assessment of elemental distribution. Figure 5a–c displays cross-sections that are ~ 15 μm in length, which are located within pristine uraninite adjacent to laser ablation pits. These pristine areas appear relatively uniform in texture, however, differences are observed with respect to the chemical composition (Fig. 5a–c). Within the Ruggles sample (Fig. 5a), there is a ~ 3.5 μm thick vertical area (right side) in which the elemental distribution is oriented distinctly as interwoven, horizontal light and dark grey regions; this may be interpreted as a result of the heat associated with the adjacent laser ablation analysis. The cross-section displayed in Fig. 5b was milled across a fracture in order to observe any potential chemical and/or structural alterations resulting from this feature. The walls along the fracture shows globular/colloform structure outlines that mimic the same overall texture of this sample (Fig. 1a). Near the top of the fissure, smaller globular pieces depict distinct core-rim textures (Fig. 5b). The colloform texture appears to have enabled the formation of several vugs of various sizes present throughout the uraninite.

Figure 5d–f is representative of altered areas for the sample of Marshall 2 uraninite. Unlike the uraninite from Ruggles, the Marshall 2 FIB cross-sections were analyzed prior to laser ablation on the sample, thus milling was conducted in close proximity to the intended LA–ICP–MS location. Cross-sections milled in Marshall 2 are longer in length, ranging from ~ 30 to 40 μm, in order to investigate larger portions due to sample macro-scale heterogeneity, and focus on boundaries between distinct textures (Fig. 5d–f); the latter is located within a Ca-rich yellow alteration rind (Fig. 5d). In the lower left corner of Fig. 5d, the uraninite displays a platy and euhedral crystal form. The left side of the SEM image illustrates blocky wedge-shaped sections containing U, Si, and Ca, likely indicating the vein is composed of uranophane ($Ca[(UO_2)(SiO_3OH)]_2{\cdot}5(H_2O)$) previously identified at this deposit by Deditius et al. [22]. In the right half of the image (Fig. 5d), there are deformed, platy uraninite segments containing Pb and S. Figure 5e depicts the cross-section milled at the intersection of a U-arsenate mineral, as indicated from EMP, and an altered uraninite. The cross section from Marshall 2 (Fig. 5e) exhibits laminar regions alternating from light to dark grey in the upper left associated with the U-arsenate. The remainder of the cross-section displays

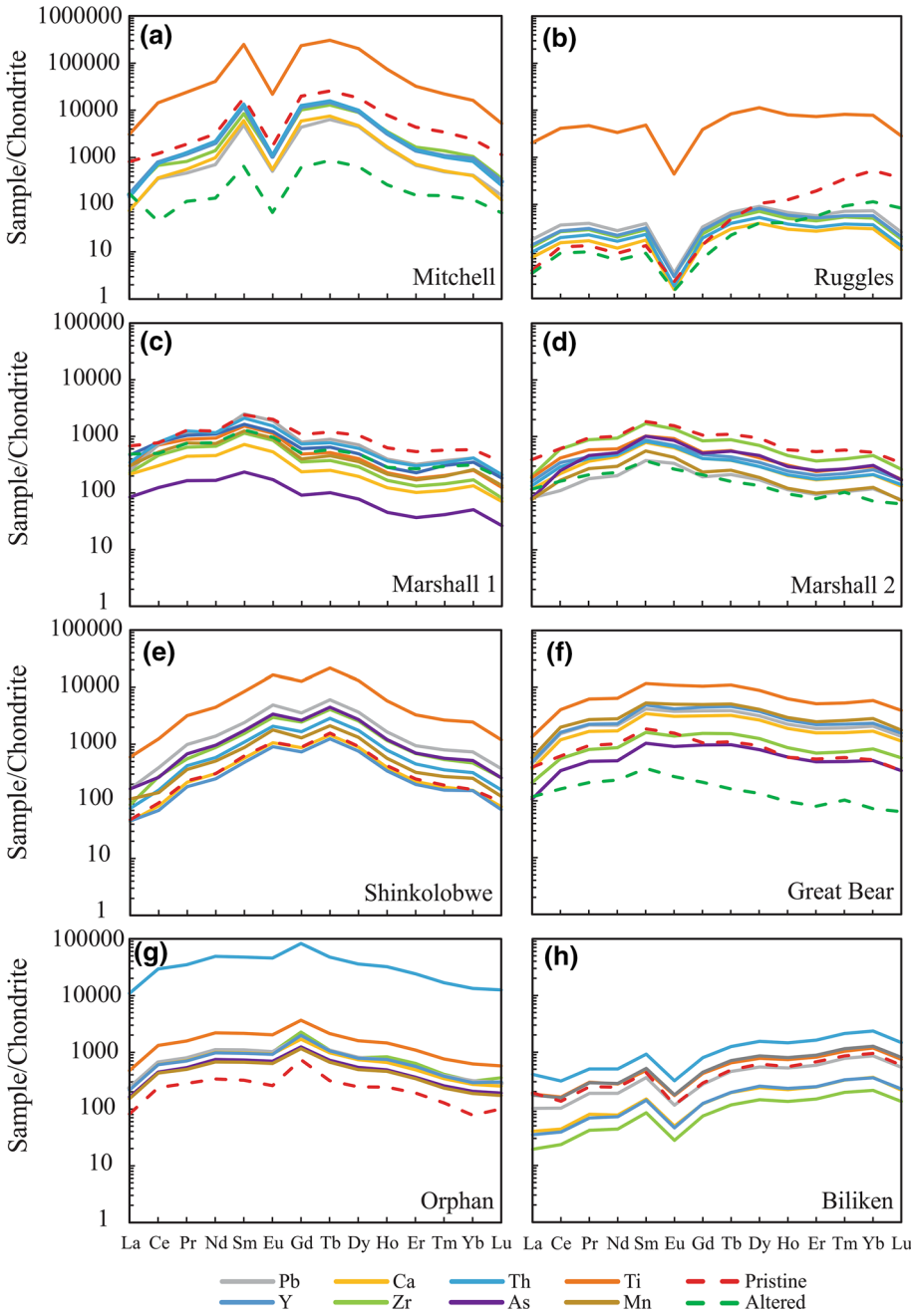

Fig. 2 The median CN–REE patterns generated by LA–ICP–MS with employing various internal standard (solid lines) are compared to CN–REE patterns determined by SM–ICP–MS (dashed lines) from optically separated pristine and altered solutions. (Color figure online)

several laminar vugs of different sizes and orientations. Lighter grey areas occur parallel to the vugs' lining and are surrounded by darker regions, which from EDS analysis contain S, W, and Pb. Within Marshall 2, Fig. 5f illustrates uraninite composed of larger segments and vugs compared to the cross section in Fig. 5e. Figure 5f also portrays the boundary between a pristine fan-shaped structure and the sample's altered matrix. The upper left portion of Fig. 5f is uniform in texture, similar to the pristine areas from Ruggles (Fig. 5a–c). This pristine section of uraninite is then truncated by large vugs, which decrease in size from left-to-right within the image. The altered uraninite displayed in Fig. 5f is similar to the deformed platy crystal forms shown in Fig. 5d.

Within the Ruggles sample, each FIB cross-section length ($\sim$ 15 μm) is half of the laser ablation diameter (30 μm) employed, and thus represents sample volume sizes of similar magnitudes. Consequently, this latter feature will ensure valid comparisons in elemental compositions obtained by both methods. EDS analyses obtained for the Ruggles sample detected solely U, Pb, and O, of which the abundances for U and Pb are negatively correlated (EDS analyses 1–15 listed in Table 4 in supplementary information). Furthermore, the average PbO content of

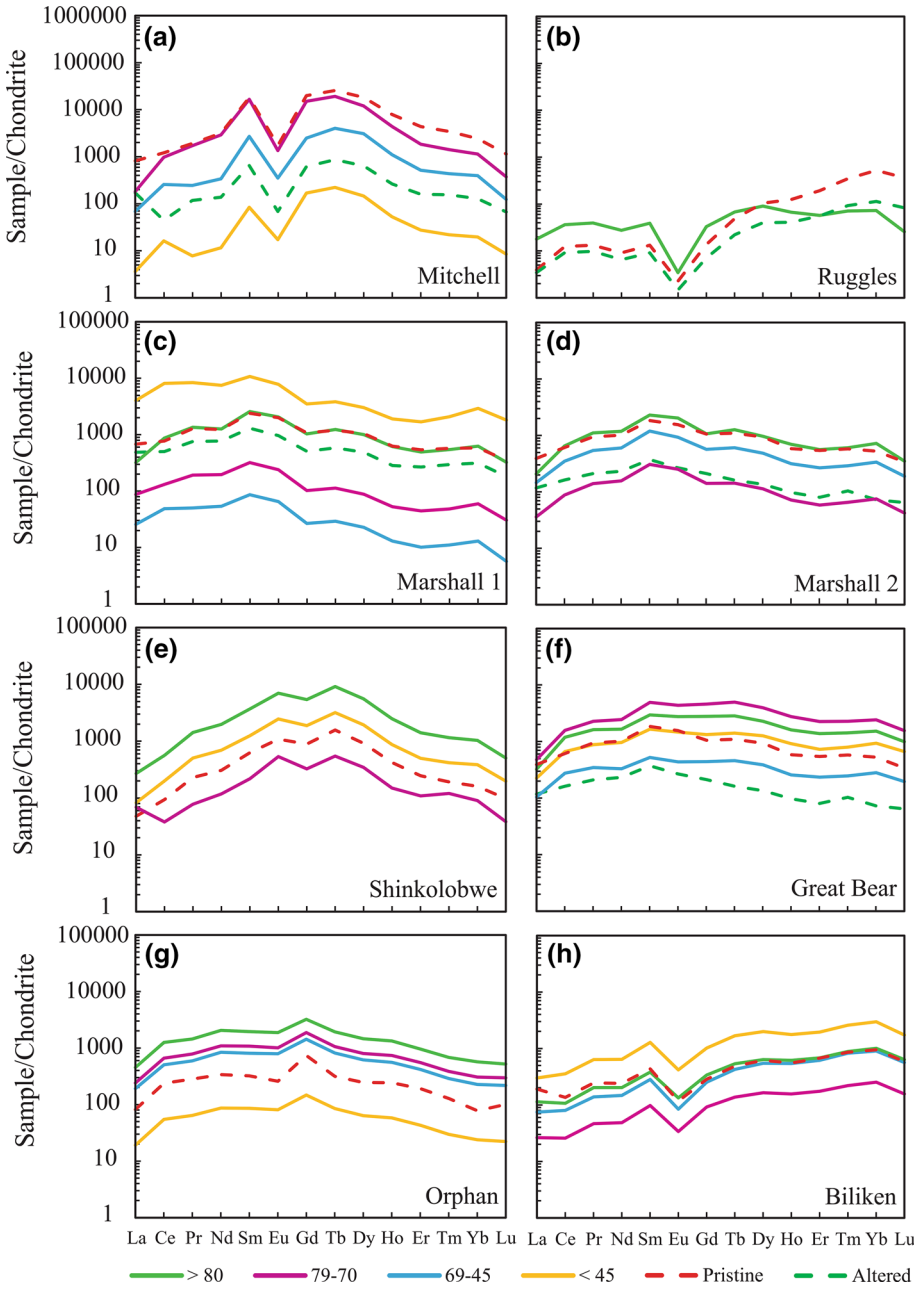

Fig. 3 CN–REE signatures determined for uraninite samples investigated here using LA–ICP–MS when Pb is employed as the internal standard and grouped according to UO_2 wt% contents: pristine > 80 (green), altered 79–70 (purple), and secondary U-minerals 69–45 (blue) and < 45 (yellow). (Color figure online)

3.94 wt% obtained by EDS is in general agreement with that measured by EMP analyses (average = 4.07 wt%) for Ruggles uraninite.

EDS analyses conducted on the cross-sections throughout the altered areas of Marshall 2 (Fig. 5d–f) indicate that the abundances of major cations (i.e., Pb, Si, S, Ca, P, As, W, Zr, Al; analyses 16–33 in Table 4 of supplementary information) are extremely variable. For example, from left-to-right (analyses 17 and 18) in Fig. 5d yield variable U, Si, and Ca contents, whereas only U, Pb, S, and Si are recorded for analysis 19 (right most position). Figure 5e illustrates the transition (left-to-right) from regions with P and As to those areas containing W, S, and Pb, W and Zr abundances are extremely variable within Marshall 2 sample (Fig. 5e, f) as these range from 0.5 to 17.7% and 0.8–13.2% respectively. The differences observed in cation incorporation is related to the numerous mineral phases present within the altered regions of the sample.

Discussion

Within the uraninite structure, uranium is typically found in its tetravalent oxidation state, however when U^{+6} is present, it allows for the incorporation of impurities that are both trivalent and divalent in nature [1]. The

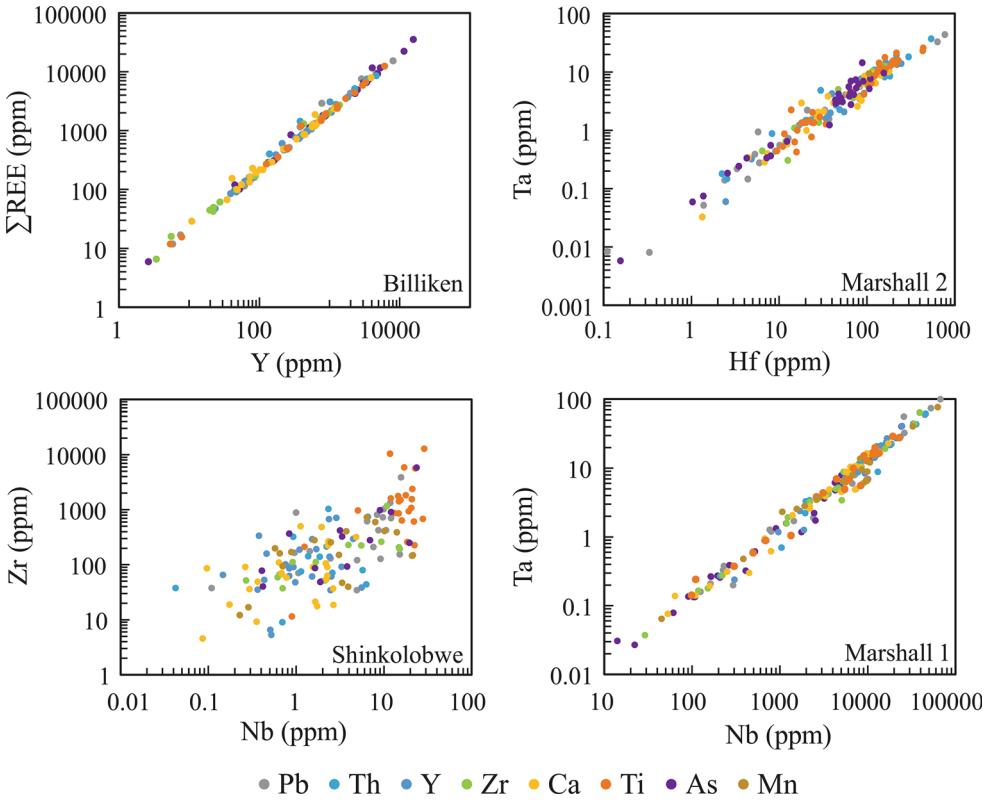

Fig. 4 Trace element concentrations (ppm) determined by LA–ICP–MS analyses using various internal standards (see text for details). (Color figure online)

composition and circulation of ore-forming fluids, often modified by host rock interactions, impact the incorporation of cations [31]. For example, Si is preferentially incorporated under reducing conditions when U is in the + 4 oxidation state [32]. Cation substitution in uraninite may also occur at the time of mineralization and is not necessarily secondary in nature [33]. Similar to other cations such as Ca, Th, and Si, Pb can be incorporated into uraninite by fluid interaction (e.g., Marshall pass deposit). However, Pb is normally incorporated within the uraninite structure from U decay, occupying interstitial sites within the uraninite structure [1]. Radiogenic Pb, initially in its + 4 oxidation state, undergoes an auto-redox reaction resulting in Pb^{+2} and the simultaneous oxidation of U^{+4} to U^{+6} [32]. This reaction can result in destabilization of the surrounding crystal structure [32], and therefore could enable increased cation substitution of other elements. Another principal cation in the structure of uraninite is Ca, which preferentially replaces U due to their similar ionic radii [31, 32].

Y and Ti are also considered important impurities within uraninite, especially since Y is geochemically similar to the REEs [32]. Contrarily, Ti is found either within accessory Ti-oxide minerals, or as inclusions within pegmatites [32]. Both of these features could explain why using Ti as an internal standard for these types of samples results in a REE signature several orders of magnitude higher than any other element used as an internal standard (Fig. 2b). It is also possible that Ti is present as Ti-oxide micro-inclusions or coatings within vugs [28], which will produce erroneous trace element concentrations obtained by LA–ICP–MS.

The abundances of other elements of interest, such as Ta, Nb, and Hf, were determined to establish if their concentrations were also affected by varying the internal standard (Fig. 4). The overlap in their respective linear arrays displayed in Fig. 4 indicate that despite variation in their absolute abundances, their relative concentrations remain constant (i.e., same ratio) regardless of the internal standard chosen.

In a recent study, Balboni et al. [34] adopted Ca and Th as internal standards for their LA–ICP–MS measurements, and compared REE abundances obtained by both LA- and SM–ICP–MS analyses for the same uraninite samples. The comparison indicates that REE concentrations measured by SM–ICP–MS analysis (subsequent the removal of U via ion exchange chromatography) are higher than those generated by LA–ICP–MS; this feature was attributed to ion signal suppression due to the U-rich matrix during the latter [34]. The spike addition method [30] adopted here for determining trace element contents by SM–ICP–MS analysis adequately monitors and corrects for matrix affects. Since the LA–ICP–MS trace element (median) abundances determined when using Pb as the internal standard are equivalent to those obtained by SM–ICP–MS for pristine

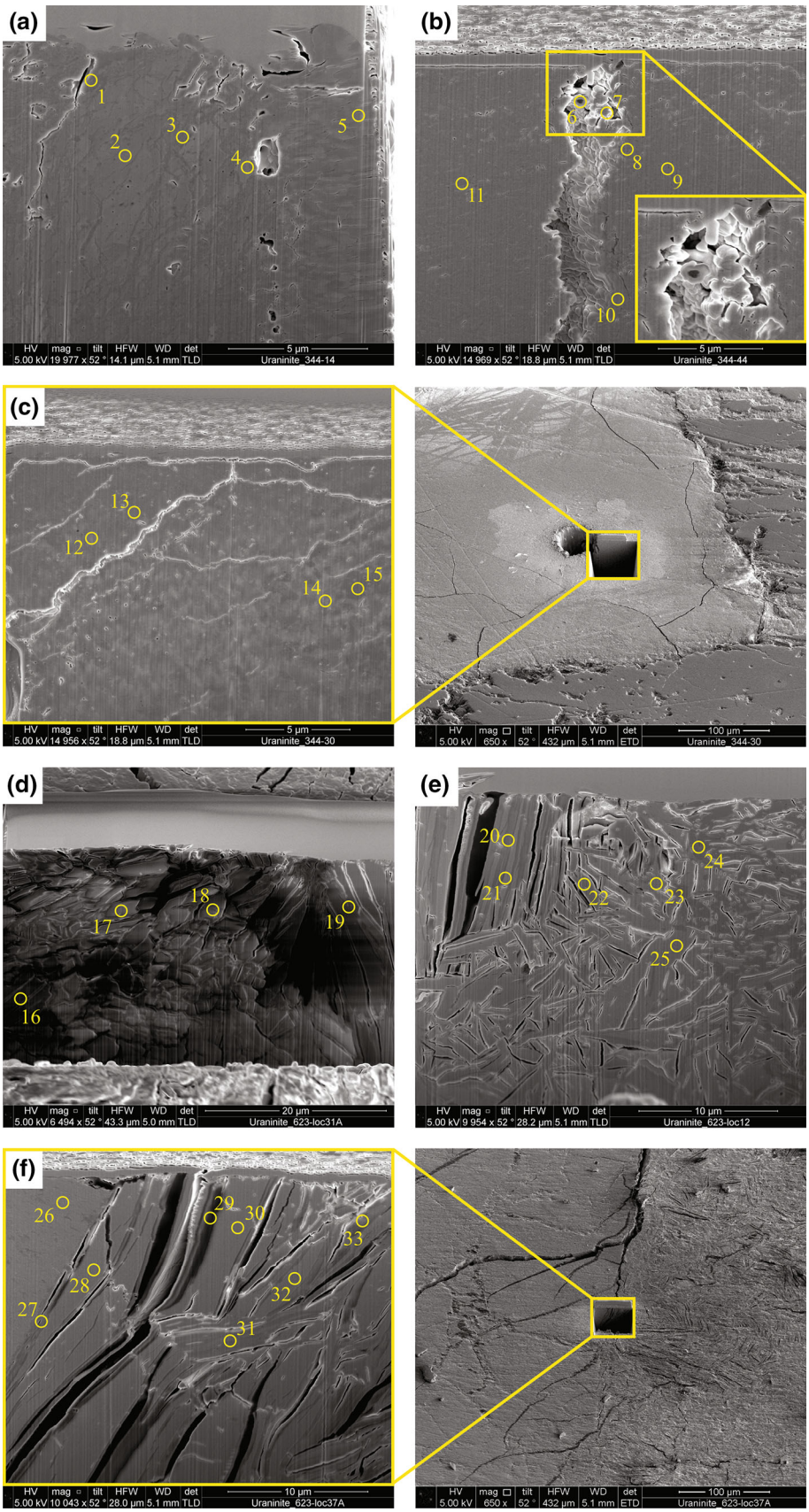

Fig. 5 FIB–SEM images of uraninite samples from Ruggles (**a**–**c**) and Marshall 2 (**d**–**f**). Numbered yellow circles indicate the location of EDS measurements and analyses are listed within Supplementary Information Table 4. (Color figure online)

fragments of uraninite (e.g., Fig. 3c, d, h), then this result suggests that the use of Pb as the internal standard may circumvent the matrix effect during LA–ICP–MS analysis; one reason for the latter may be related to its similar mass to that of U, and hence similar ionization behavior within the plasma environment of an ICP–MS instrument. Moreover, the distribution of Pb within each sample was carefully evaluated by detailed EMP analyses prior to LA–ICP–MS measurements, and the pertinent PbO wt% values were adopted within the GLITTER data reduction software for areas investigated.

The grouping of laser ablation analyses based on the amount of UO_2 (> 80, 79–70, 69–46, and < 45 wt%) provides insight into how the removal of U (or degree of alteration) affects the overall trace element signature of uraninite. The ability of secondary minerals to incorporate REEs is influenced by the overall crystalline nature and composition of the alteration phase(s) [34]. This is further supported by the observations within this study that secondary U minerals contain variable (higher or lower) REE contents compared to those corresponding to pristine areas of uraninite. For example, the concentrations of REEs decrease as the amount of UO_2 decreases (i.e., areas with increased alteration show depletion in REEs) for the uraninite from Mitchell (Fig. 3a), whereas the opposite trend is observed for the sample from Billiken (Fig. 3h).

The REE signatures obtained by SM–ICP–MS analysis for pristine sections of uraninite (> 80 wt% UO_2) from Marshall 1 and 2 and Billiken match those determined by LA–ICP–MS when using Pb as the internal standard (Fig. 3 c, d, h). Moreover, the median CN–REE pattern obtained for uraninite with 70–79 wt% UO_2 from Marshall 2 obtained by LA–ICP–MS analyses when using Pb as the internal standard coincides with that for altered sections measured by SM–ICP–MS analysis (Fig. 3d). Therefore, this result suggests that 'altered' uraninite from Marshall 2 is a major constituent phase, and is corroborated by the fact that the calculated, median abundance of UO_2 in this sample is 78 wt% based on EMP analyses (Table 1 in supplementary information). The SM–ICP–MS pristine signatures for uraninite samples from Mitchell and Great Bear correspond with those for the LA–ICP–MS determined signatures of altered and secondary U-bearing regions, respectively, when Pb is adopted as the internal standard (Fig. 3a, f). These bulk SM–ICP–MS signatures could be influenced by the fractured nature of the uraninite for both samples, which may contain altered uraninite and secondary-U minerals (Supplementary Fig. 1). Ruggles uraninite shows an enrichment in the heavy REEs for the SM–ICP–MS CN pattern for both pristine and altered solutions (Figs. 2, 3b), which is not as apparent for the LA–ICP–MS analyses. This heavy REE enrichment is most likely associated with the inclusion of fine-grained zircon in the powdered, bulk sample that was prepared for solution mode analyses (Fig. 1a and Supplementary Fig. 2). Due to the large-scale heterogeneity within the Shinkolobwe and Orphan samples, it was not possible to separate pristine from altered/secondary regions as with the other samples. Therefore, the resulting SM–ICP–MS analyses for pristine aliquots from these two samples yield lower REE abundances compared to their respective LA–ICP–MS measurements of pristine areas, which most likely reflect a mixed composition (pristine and altered; Fig. 3f, g). Most importantly, all REE signatures, irrespective of whether obtained by LA- or SM–ICP–MS analysis, demonstrate that the shape of the CN–REE patterns for each sample remains constant, and is unaffected by alteration or the internal standard used (Figs. 2, 3).

Of interest, the CN–REE patterns generated by LA–ICP–MS analyses indicate significant variability between individual spots within pristine sections. For example, all LA–ICP–MS analyses conducted on the Ruggles uraninite sample are from pristine regions; however, the CN–REE signatures vary an order of magnitude utilizing the same internal standard (Lewis, unpublished data). The chemical heterogeneity that is illustrated within single FIB cross-sections for both Ruggles and Marshall 2 uraninites (Fig. 5) supports the importance of determining a proper internal standard for laser ablation and highlights the increasing chemical complexity as a result of alteration processes. The FIB cross-sections conducted on three altered sections within Marshall 2 show a range of textures in relation to the growth of the secondary-U minerals, such as blocky wedge, laminar, pristine and deformed platy-shaped structures. Vug sizes within the altered cross-sections (Marshall 2, Fig. 5d–f) are larger and more prevalent than evidenced within pristine areas (Ruggles, Fig. 5a–c). Lastly, EDS analyses detected solely U, Pb, and O in pristine regions of uraninite, which corroborates the interpretation that Pb is a major chemical constituent and can be considered an optimal internal standard when conducting in situ LA–ICP–MS analyses of this mineral.

One important feature that must be considered when using Pb as the internal standard for LA–ICP–MS analysis of uraninite is that a correction factor must be applied to the PbO wt% (obtained by EMP) before it is used in the GLITTER data reduction software. The GLITTER software assumes the PbO wt% content is of natural isotopic abundance (^{208}Pb = 52.3%, ^{207}Pb = 22.08%, ^{206}Pb = 24.14%, and ^{204}Pb = 1.42%). However, the radiogenic Pb component contained within uraninite may be significant and if not taken into consideration, will result in erroneous calculated REE concentrations (Fig. 6). Thus, a correction factor should be calculated for each sample, and it becomes increasingly important with increasing geological age of the uraninite investigated. The correction

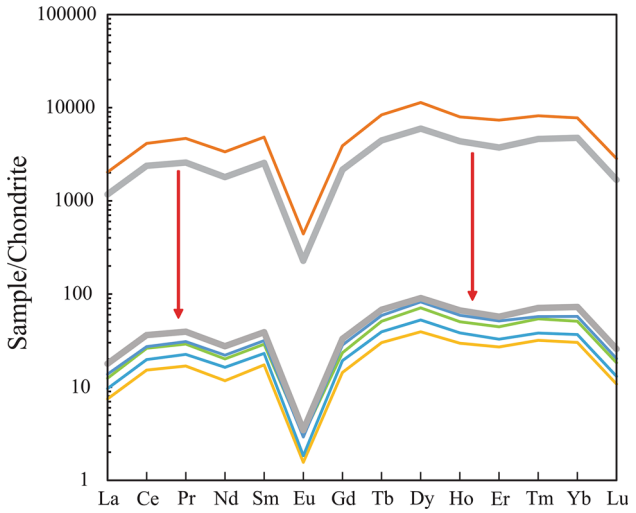

Fig. 6 CN–REE patterns for LA–ICP–MS analyses of Ruggles uraninite that illustrate the effect of the Pb isotope composition adopted within GLITTER data reduction software. The grey CN–REE pattern located at the top of the diagram represents results obtained when an uncorrected, natural Pb isotopic abundance is employed, whereas the grey CN–REE pattern at the bottom used the sample's measured Pb isotope ratios

factor is determined by calculating the relative abundances of the Pb isotopes within the uraninite based on measured Pb isotopic values obtained by SM–MC–ICP–MS for the samples examined here (Lewis, unpublished data). The relative homogeneity of the Pb isotope ratios obtained by SM–MC–ICP–MS was verified by conducting in situ LA–MC–ICP–MS measurements on the same samples (Lewis, unpublished data). The calculated relative content of ^{208}Pb is then divided by the natural abundance of ^{208}Pb, and the ratio of true/natural is then multiplied with the PbO wt% obtained from EMP, which yields the correct value for input into GLITTER. As an example, the change in the position of the CN–REE pattern for the Ruggles uraninite corresponding to results obtained both prior and subsequent the application of the correction factor for Pb is depicted in Fig. 6.

Conclusions

The rapid and accurate characterization of the chemical and isotopic signatures of uraninite, the main ore mineral used for U-based fuel, is currently a critical goal of nuclear forensic investigations. FIB–SEM investigations conducted here of what appear at the surface to be pristine sections of uraninite suggest that significant internal chemical and textural heterogeneity is present. Similarly, analyses of altered areas illustrate highly variable elemental concentrations and crystal morphologies evidenced by complex subsurface textures. Here, Pb is recommended as the ideal internal standard element for laser ablation analyses of uraninite. EDS spectra indicate that only U, Pb, and O are present as major chemical constituents within pristine areas of uraninite, and hence confirm Pb as the ideal element to use as the internal standard for LA–ICP–MS analyses. Pb is an intrinsic element within the uraninite structure as it is primarily produced from the decay of U. The results reported here demonstrate that even if Pb has been either removed or added to uraninite, LA–ICP–MS analyses of a pristine area can still produce a CN–REE signature equivalent to that corresponding to the SM–ICP–MS analysis of a pristine bulk sample (e.g., Marshall 1 and 2). CN–REE patterns obtained by LA–ICP–MS analyses vary several orders of magnitude but their shapes remain constant for each sample. The importance of the FIB investigations conducted here, which are comparable in size to the laser ablation spots employed, is demonstrated by the identification of vugs that may contain micro-inclusions within pristine uraninite. In turn, these may be partly responsible for the large variation in calculated trace element abundances.

When using Pb as an internal standard for LA–ICP–MS investigations of uraninite, the resultant CN–REE signatures were grouped on the basis of their UO_2 concentrations. This grouping indicates that LA–ICP–MS analysis of pristine areas (> 80 wt% UO_2) produces a CN–REE signature that coincides with the corresponding pattern established using bulk SM–ICP–MS analysis of pristine sections of the same sample. However, when using Pb as the internal standard, the radiogenic nature of Pb within uraninite and its corresponding isotopic composition must be considered prior to use of the GLITTER data reduction software in order to obtain accurate results. For uraninites characterized by low Pb abundances, then Ca or Th may be substituted as the internal standards for LA–ICP–MS analyses since these elements yield similar trace element concentrations compared to those obtained for Pb.

Acknowledgements Funding for this project was provided by the Department of Homeland Security (Grant# 2014-DN-077-ARI082). The authors thank Dr. Ian Steele for his help and expertise with operation of the EMP and to Notre Dame's Center of Environmental Science and Technology (CEST) for use of the μ-XRF. Lawrence Livermore National Laboratory is operated by Lawrence Livermore National Security, LLC, for the U.S. Department of Energy, National Nuclear Security Administration under Contract DE-AC52-07NA27344.

References

1. Janeczek J, Ewing RC (1992) Structural formula of uraninite. J Nucl Mater 190:128–132
2. Hore-Lacy I (2016) Uranium for nuclear power: resources, mining and transformation to fuel. Woodhead Publishing, Sawston

3. Frimmel HE, Schedel S, Brätz H (2014) Uraninite chemistry as forensic tool for provenance analysis. Appl Geochem 48:104–121. https://doi.org/10.1016/j.apgeochem.2014.07.013
4. Spano TL, Simonetti A, Balboni E, Dorais C, Burns PC (2017) Trace element and U isotope analysis of uraninite and ore concentrate: applications for nuclear forensic investigations. Appl Geochem 84:277–285. https://doi.org/10.1016/j.apgeochem.2017.07.003
5. Uvarova YA, Kyser TK, Geagea ML, Chipley D (2014) Variations in the uranium isotopic compositions of uranium ores from different types of uranium deposits. Geochim Cosmochim Acta 146:1–17. https://doi.org/10.1016/j.gca.2014.09.034
6. Spano TL, Simonetti A, Wheeler T, Carpenter G, Freet D, Balboni E, Dorais C, Burns PC (2017) A novel nuclear forensic tool involving deposit type normalized rare earth element signatures. Terra Nova. https://doi.org/10.1111/ter.12275
7. Mercadier J, Cuney M, Lach P, Boiron M, Bonhoure J, Richard A, Leisen M, Kister P (2011) Origin of uranium deposits revealed by their rare earth element signature. Terra Nova. https://doi.org/10.1111/j.1365-3121.2011.01008.x
8. Balboni E, Jones N, Spano T, Simonetti A, Burns PC (2016) Chemical and Sr isotopic characterization of North America uranium ores: nuclear forensic applications. Appl Geochem 74:24–32. https://doi.org/10.1016/j.apgeochem.2016.08.016
9. Varga Z, Wallenius M, Mayer K, Meppen M (2011) Analysis of uranium ore concentrates for origin assessment. Proc Radiochim Acta 1:1–4. https://doi.org/10.1524/rcpr.2011.0004
10. Bellucci JJ, Simonetti A, Koeman EC, Wallace C, Burns PC (2014) A detailed geochemical investigation of post-nuclear detonation trinitite glass at high spatial resolution: delineating anthropogenic vs. natural components. Chem Geol 365:69–86. https://doi.org/10.1016/j.chemgeo.2013.12.001
11. Dustin MK, Koeman EC, Simonetti A, Torrano Z, Burns PC (2016) Comparative investigation between in situ laser ablation versus bulk sample (solution mode) inductively coupled plasma mass spectrometry (ICP-MS) analysis of trinitite post-detonation materials. Appl Spectrosc 70:1446–1455
12. Lach P, Mercadier J, Dubessy J, Boiron MC, Cuney M (2013) In situ quantitative measurement of rare earth elements in uranium oxides by laser ablation-inductively coupled plasma-mass spectrometry. Geostand Geoanal Res. https://doi.org/10.1111/j.1751-908X.2012.00161.x
13. Depiné M, Frimmel HE, Emsbo P, Koeng AE (2013) Trace element distribution in uraninite from Mesoarchaean Witwatersrand conglomerates (South Africa) supports placer model and magmatogenic source. Miner Depos 48:423–435. https://doi.org/10.1007/s00126-013-0458-3
14. Zhao D, Ewing RC (2000) Alteration products of uraninite from the Colorado Plateau. Radiochim Acta 88:739–749
15. Wirth R (2009) Focused ion beam (FIB) combined with SEM and TEM: advanced analytical tools for studies of chemical composition, microstructure and crystal structure in geomaterials on a nanometre scale. Chem Geol 261:217–229. https://doi.org/10.1016/j.chemgeo.2008.05.019
16. Simonetti A, Heaman LM, Hartlaub RP, Creaser RA, MacHattie TG, Böhm C (2005) U–Pb zircon dating by laser ablation-MC-ICP-MS using a new multiple ion counting Faraday collector array. J Anal Atom Spectrom 20:677–686. https://doi.org/10.1039/b504465k
17. Schurr MR, Donohue PH, Simonetti A, Dawson E (2018) Multi-element and lead isotope characterization of early nineteenth century pottery sherds from Native American and Euro-American sites. J Archaeol Sci Rep 20:390–399
18. Miller RG (1982) The geochronology of uranium deposits in the Great Bear Batholith, Northwest Territories. Can J Earth Sci. 19:1428–1448
19. Decrée S, Deloule É, De Putter T, Dewaele S, Mees F, Yans J, Marignac C (2011) SIMS U–Pb dating of uranium mineralization in the Katanga Copperbelt: constraints for the geodynamic context. Ore Geol Rev 40:81–89. https://doi.org/10.1016/j.oregeorev.2011.05.003
20. Dahlkamp FJ (1991) Uranium ore deposits. Springer, Berlin
21. Cuney M (2009) The extreme diversity of uranium deposits. Miner Depos 44:3–9. https://doi.org/10.1007/s00126-008-0223-1
22. Deditius AP, Utsunomiya S, Ewing RC (2007) Fate of trace elements during alteration of uraninite in a hydrothermal vein-type U-deposit from Marshall Pass, Colorado, USA. Geochim Cosmochim Acta 71:4954–4973. https://doi.org/10.1016/j.gca.2007.08.008
23. Brobst DA (1962) Geology of the Spruce Pine District, Avery, Mitchell, and Yancey Counties, North Carolina. US Government Printing Office, Washington, DC
24. Korzeb SL, Foord EE, Lichte FE (1997) The chemical evolution and paragenesis of uranium minerals from the Ruggles and Palermo granitic pegmatites, New Hampshire. Can Miner 35:135–144
25. Shaub BM (1938) The occurrence, crystal habit and composition of the uraninite from the Ruggles Mine, near Grafton Center, New Hampshire. Am Miner 23:334–341
26. Olson JC (1941) Mica-bearing Pegmatites of New Hampshire. US Government Printing Office, Washington, DC
27. Granger HC, Raup RB (1962) Reconnaissance study of uranium deposits in Arizona. US Government Printing Office, Washington, DC
28. Burns PC, Finch R (1999) Uranium: mineralogy, geochemistry and the environment. Mineralogical Society of America, Chantilly
29. van Achterbergh E, Ryan CG, Jackson SE, Griffin WL (2001) Data reduction software for LA–ICP–MS: appendix. In: Sylvester PJ (ed) Laser ablation–ICP–mass spectrometry in the earth sciences: principles and applications, vol 29. Short course series. Mineralogical Association of Canada, Quebec
30. Jenner GA, Longerich HP, Jackson SE, Fryer BJ (1990) ICP-MS A powerful tool for high-precision trace-element analysis in Earth sciences: evidence from analysis of selected U.S.G.S. reference samples. Chem Geol 83:133–148. https://doi.org/10.1016/0009-2541(90)90145-W
31. Alexandre P, Kyser KT (2005) Effects of cationic substitutions and alteration in uraninite. Can Miner 43:1005–1017
32. Finch RJ, Murakami T (1999) Systematics and paragenesis of uranium minerals. In: Burns PC, Ewing RC (eds) Uranium: mineralogy and geochemistry, vol 38. Mineralogical Society of America, Chantilly, pp 91–179
33. Alexandre P, Kyser K, Layton-Matthews D, Joy B, Uvarova Y (2015) Chemical compositions of natural uraninite. Can Miner. https://doi.org/10.3749/canmin.1500017
34. Balboni E, Simonetti A, Spano T, Cook ND, Burns PC (2017) Applied geochemistry rare-earth element fractionation in uranium ore and its U(VI) alteration minerals. Appl Geochem 87:84–92. https://doi.org/10.1016/j.apgeochem.2017.10.007